Mesophase Transitions in [(C₂H₅)₄N][FeBrCl₃] and [(CH₃)₄N][FeBrCl₃] Ferroic Plastic Crystals

Julian Walker,* Kenneth P. Marshall, Jorge Salgado-Beceiro, Benjamin A. D. Williamson, Nora S. Løndal, Socorro Castro-Garcia, Manuel Sánchez Andújar, Sverre M. Selbach, Dmitry Chernyshov, and Mari-Ann Einarsrud
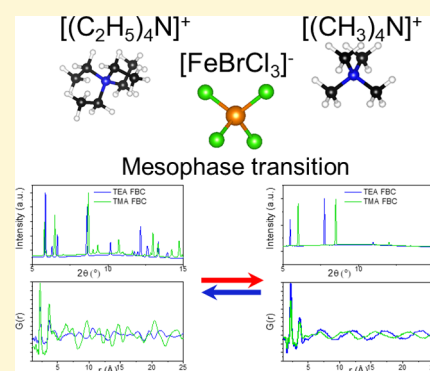
ABSTRACT: Plastic crystals are supramolecular materials that possess a unique high entropy mesophase at elevated temperatures, where a long-range structural symmetry coexists with a local molecular orientational disorder. The transition to mesophase can involve a large entropy change useful for thermal energy storage and influences the temperature range of ferroelectric and piezoelectric properties, important for sensor applications. Synchrotron X-ray diffraction and pair distribution function analysis were used to study the structure, while calorimetry, dielectric, leakage current measurements, and density functional theory were used to investigate the influence of the organic cation on the structure and properties of tetraethylammonium bromotrichloroferrate(III) $[(C_2H_5)_4N][FeBrCl_3]$ and tetramethylammonium bromotrichloroferrate $[(CH_3)_4N][FeBrCl_3]$. The $[(C_2H_5)_4N][FeBrCl_3]$ mesophase transition had an entropy change of $151.5 \, J \cdot K^{-1} \cdot kg^{-1}$, while $[(CH_3)_4N][FeBrCl_3]$ had only $49 \, J \cdot K^{-1} \cdot kg^{-1}$. This was explained by the $[(C_2H_5)_4N][FeBrCl_3]$ mesophase having less long-range structural symmetry and more local orientational disorder, of both the cations and anions, compared to $[(CH_3)_4N][FeBrCl_3]$. Both materials exhibited at least two conductive mechanisms below the transition, vacancy-mediated ionic and electronic conduction. The introduction of anion orientational freedom, as opposed to cation orientational freedom, at the mesophase transition was most influential for the electrical properties.

INTRODUCTION

Plastic crystals are a class of supramolecular materials defined by their combination of long-range crystallographic order and local structural disorder.[1−6] The long-range structure determines the structural symmetry and creates properties such as ferroelectricity and piezoelectricity,[1−4] while the local disorder arises from the orientational freedom of individual molecules,[5] causing entropy increases,[6,7] unit cell expansion, and increased ionic conductivity.[8] The molecular orientational freedom in plastic crystals is strongly temperature-dependent and is determined by the molecular chemistry, shape, and intermolecular bonding.[5] The temperature dependence of the orientational freedom means that plastic crystals enter a mesophase state prior to melting, in which the molecules exhibit a maximum orientational freedom for the solid state, but still maintain fixed positions in the crystal lattice. The onset of this structural phase is marked by a solid-to-mesophase transition which usually involves a very large entropy change.[5−7]

Plastic crystals are water-soluble alternatives to metal oxide ferroelectrics that are processable at low temperatures and thus have potential for complementary metal oxide semiconductor compatibility and improved recyclability.[9−11] The organic

molecular species in plastic crystals may be used to tailor the structure and properties without significantly increasing the number of different periodic table elements used, and thus, could help to combat the challenge of compositional complexity, which constitute a sustainability problem for state-of-the-art electronics.[8,12,13]

The large entropy change at the mesophase transition makes plastic crystals with organic and inorganic molecules interesting for thermal energy storage (TES).[6,14] The mesophase has a higher density compared to a liquid without being susceptible to leaking, and the inorganic molecules in the composition provide increased thermal stability. Plastic crystals therefore have the potential for improved safety and efficiency in solid-state cooling.

This work explores the temperature-dependent structure and thermodynamic and electrical properties of two plastic crystal
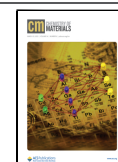
ferroic materials based on the inorganic molecular anion bromotrichloroferrate(III) $[FeBrCl_3]^-$ and two different organic cations, tetraethylammonium $[(C_2H_5)_4N]^+$ and tetramethylammonium $[(CH_3)_4N]^+$. The mixed halide anion was chosen over its $FeCl_4$ analogue for several reasons. The addition of the Br varies the bond lengths of one of the four tetrahedral positions, resulting in a disruption of the $3m$ symmetry of the tetrahedral molecule.[15] This kind of disruption to the local molecular symmetry also plays a role in the stability of the long-range crystal structure. In ferroic materials, cations are often substituted in the structure to form solid solutions as a means of destabilizing the crystal structure, which can result in the enhancement of dielectric constants and electromechanical properties. Similar solid solution approaches have also been shown to be effective approaches for property engineering in hybrid perovskites.[16] In the case of the Br substitution for Cl in the tetrahedral anion in these compositions, it has been shown that the introduction of a single Br increases the entropy of the mesophase transition, increases the remanent polarization of ferroelectric hysteresis loops, and increases the strength of magnetic interactions.[17,18] Adjusting the halide composition with a solid solution approach is thus a useful means of modifying key material properties.

The two cation species were chosen because they create significant structural differences.[11,15,17] Tetraethylammonium bromotrichloroferrate(III) $[(C_2H_5)_4N][FeBrCl_3]$, TEA FBC, exhibits a large entropy change across the mesophase transition and has a hexagonal structure (space group $P6_3mc$, no. 186).[15,18] It is isosymmetric with the commercially significant AlN piezoelectric utilized for radio frequency antenna applications (Figure 1a).[19,20] Tetramethylammonium
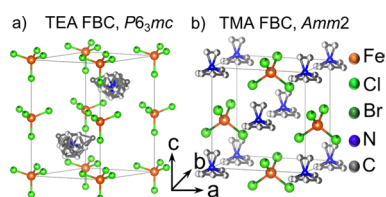
Figure 1. Structural models of the unit cells of TEA FBC and TMA FBC. Equivalent positions of carbon atoms are included with half-filled spheres reflecting the site occupancy. Br and Cl have the same sites. H atoms are not shown.[15,17]

bromotrichloroferrate(III) $[(CH_3)_4N][FeBrCl_3]$, TMA FBC, was recently identified with an orthorhombic crystal structure (space group $Amm2$, no. 38) (Figure 1b) and promising multiaxial ferroelectric polarization, substantial electromechanical strains, and a promising piezoelectric coefficient of 110 pC/N.[11,17] These properties make both materials interesting for applications, but the relationship between the composition, structure, and properties are not well understood.

Understanding how the compositional differences impact the transition temperature, entropy, and structural and electrical characteristics in the vicinity of the mesophase transition is of particular importance as this underpins the materials' usefulness as a caloric material for TES and the temperature range over which they can function as effective ferroelectrics or piezoelectrics.[3,7,12] Determining the effect that the organic molecular cation has on the structure and properties of these two plastic crystals is an important part of a larger effort to establish effective compositional engineer-

ing strategies to further develop plastic crystal ferroics for specific applications.[21]

■ EXPERIMENTAL METHODS

TEA FBC was prepared by dissolving precursors tetraethylammonium bromide (99 wt %, Sigma-Aldrich, USA) and iron(III) trichloride hexahydrate (97 wt %, Sigma-Aldrich, USA) in deionized (DI) water. The solution was allowed to evaporate at room temperature for 7 days after which the solidified crystals were separated from the remaining solution by vacuum filtration and dried in vacuum at 60 °C.

TMA FBC was prepared by dissolving tetramethylammonium bromide (98 wt %, Sigma-Aldrich, USA) and iron(III) trichloride hexahydrate in DI water. The water was reduced by evaporation in a rotary evaporator at 70 °C. Once reduced to 20% of the original volume, the remaining solution was vacuum filtered. The solid was redissolved in ethanol (99.999 wt %, Sigma-Aldrich, USA) at 70 °C. The solution was allowed to cool to room temperature, usually left for 24 h, and the crystalline solid was filtered from the solution by vacuum filtration and dried in vacuum at 60 °C.

Differential scanning calorimetry (DSC) was performed with a DSC 214 Polyma (NETZSCH, Germany) between −25 and 200 °C with heating and cooling rates of 10 °C/min and a hold time of 15 min at minimum and maximum temperatures. Measurements were conducted in synthetic air with closed Al crucibles (NETZSCH, Germany). Three thermal cycles were completed continuously for each measurement.

For X-ray diffraction (XRD) experiments, the plastic crystals were crushed into a powder using a mortar and pestle and filled into 0.3 mm diameter quartz capillaries (Test Capillary Suppliers, United Kingdom). Powder XRD experiments were conducted at the Swiss Norwegian Beam Lines (SNBL), beam line BM01, European Synchrotron Radiation Facility (ESRF). A wavelength of 0.73074 Å was used together with a Pilatus 2M detector (Dectris, Switzerland). A mask was used to eliminate the signal below 12 keV to reduce the noise caused by fluorescence from the Br. A 250 mm Al attenuator was used to prevent radiation damage of the samples. Capillaries containing the materials were mounted on a goniometer head with thermal wax and rotated through 45° during the data acquisition at each temperature. For both X-ray experiments the temperature was controlled with a hot-air blower mounted directly above the capillary and calibrated using thermocouples at the blower tip and inside a test capillary.

Fitting of diffraction profiles was performed with Topas (Bruker AXS, Germany) in an open script format[22] using an $Amm2$ model from Cambridge crystallographic data center (CCDC) file 1574204, $Cmcm$ model CCDC file 1574207 from Harada et al.,[17] and $P6_3mc$ structure from Evans et al.[15] The high-temperature structure of both materials was fit using a $Pm\bar{3}m$ centrosymmetric cubic space group with a single Fe ion located at the body center position tetrahedrally coordinated by Cl/Br positions and N located at the corners tetrahedrally coordinated by C. Two sets of equivalent tetrahedral positions were used for both the Cl/Br and C atoms and the occupancy adjusted to 50% to maintain stoichiometry.

Total scattering measurements were conducted at X-ray Radiation source PETRA III, beam line P21.2 using a wavelength of 0.18673 Å. A Varex 4 detector (Varex Imaging Corporation, USA) was also used. A custom-designed capillary holder was used to mount samples, and capillaries were not rotated during the measurement. $S(Q)$ calculation and Fourier transforms were done with PDFgetx3.[23] The background was taken from an empty capillary, and nickel was used as a standard to obtain Q_{damp} and Q_{broad}, and a Q_{max} of 20 Å^{-1} was used. Pair distribution functions (PDFs) over distances of 100 Å were produced. The temperature profile was 0.2 °C/s heating from room temperature to 200 °C, followed by a 30 min hold, and 0.4 °C/s cooling from 200 °C to room temperature.

PDF fitting was performed with DiffPy-CMI using a small box/Rietveld-like method.[24] Below the mesophase the same structural models were used as for the XRD data fitting. For the mesophase structures, however, a slight modification was made. Only one set of

tetrahedral positions was used for the Cl/Br and C atoms of each molecule. This enabled a better fit to the intensities of peaks associated with the Cl/Br−Cl/Br distances <4 Å. As a result, the structural symmetry of the mesophase structural model was reduced and the space group became $P\bar{4}3m$.

During fitting, the lattice parameters, C and Cl/Br atomic positions were first refined using the entire $G(r)$ region from 0 to 50 Å. Afterward, the lattice parameters, C and Cl/Br atomic positions were fixed to the same values for all regions. The PDFs were then divided into two $G(r)$ regions, <5 and 5−50 Å, coinciding approximately with the intramolecular and intermolecular atomic pair distances, respectively. The thermal parameters were then refined for each region separately using the U_{iso} factor for the Fe and N positions and the U_{11} and U_{12} factors for Cl/Br and C positions, respectively. The refinement of the thermal factors has been used in the literature to allow the fitting of mesophase structures above 5 Å.[25]

Density functional theory (DFT) calculations were performed with the Vienna ab initio simulation package (VASP)[26−29] using the Perdew−Burke−Ernzerhof (PBE)[30] and PBEsol[31] functionals and the projector-augmented wave method.[32] A Hubbard U[33] value of 4 eV was applied to Fe 3d states based on the previous work on Fe_2O_3.[34] Spin-polarized calculations were carried out with antiferromagnetic ordering imposed on the Fe sublattices of both TEA FBC and TMA FBC compounds. Due to the highly rotationally disordered nature of these compounds, structure determination was carried out by encompassing all symmetry inequivalent unique 90° rotations of either the $[(CH_3)_4N]$ or the $[(C_2H_5)_4N]$ cations within the $Amm2$ and $P6_3mc$ cells, respectively. The anion was approximated as a $[FeCl_4]$ (FC) ion to simplify and reduce the large configurational parameter space. This resulted in 32 and 20 configurations for TMA FC and TEA FC compounds, respectively. For both systems, all rotational configurations were found to be <0.01 eV atom[−1] of each other and thus were all included in the analysis.

Structural optimizations of the bulk unit cells were performed allowing atomic positions, cell angle, and lattice vectors to freely relax until the forces on all ions were less than 0.01 eV Å^{−1}. A plane-wave energy cutoff of 500 eV and a Monkhorst−Pack k-point meshes of 2 × 2 × 2 were used for all configurations.

Density functional perturbation theory (DFPT) was used to calculate the static dielectric constants of TEA and TMA on each rotational configuration.[35] Although it is acknowledged that molecular rotations play an active role in determining the static dielectric constant at low frequencies in MAPI,[36] DFPT provides a reasonable and computationally feasible approximation for comparison with experiments.[37]

For electrical measurements, polycrystalline samples were prepared by crushing crystals with a mortar and pestle before hot pressing at 140 °C and approximately 10 MPa in a uniaxial hot press. Gold electrodes were sputtered onto samples using a shadow mask to give electrical test specimen dimensions of approximately 3 mm diameter and 0.2 mm thickness. Dielectric spectroscopy was conducted with a thermally controlled ProboStat impedance analyzer (Novotherm, Germany). DC current voltage measurements were conducted with a Tf analyzer (aixACCT, Germany), a thermally controlled sample stage, and a TREK 10 kV signal amplifier. The current was measured as a function of applied electric field between −5 and 5 kV/cm, over temperatures ranging from 25 to 150 °C. A 30 s delay between voltage application and current measurement was used to allow for capacitance dissipation. The maximum temperature was limited by a dielectric breakdown.

■ RESULTS AND DISCUSSION

Thermodynamic Analysis. DSC provides a fingerprint of the material's heat capacity and the thermodynamic changes taking place. Figure 2 shows the heat flow for TEA FBC and TMA FBC. One clear phase transition is found in TEA FBC in the temperature range −15 to 200 °C (Figure 2a), consistent with the literature, although additional transitions are known to occur at lower temperatures.[15,38] On heating, the phase
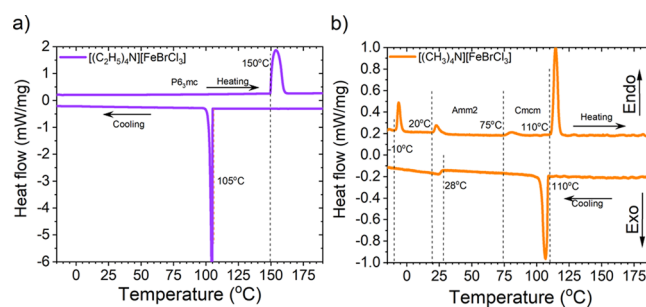
Figure 2. DSC between −15 and 190 °C for (a) TEA FBC and (b) TMA FBC. Heating and cooling direction are labeled together with the phase transition onset temperatures which are marked with dashed lines.

transition from solid to mesophase took place at 149 °C. A hysteresis of 44 °C was observed with the reverse transition taking place at 105 °C on cooling. On heating, the transition took place over an approximately 20 °C temperature window, while the transition was more rapid on cooling, completing in under 10 °C. This is reflected by the full width half-maximum (fwhm) of the transition peak (Table 1).

Table 1. Key Thermodynamic Parameters of the Mesophase Transition Determined from DSC

	TEA FBC	TMA FBC
peak onset, heating (°C)	149	109
heating ΔH (J·g^{-1})	65.7	19
heating ΔH (J·mol^{-1})	24.5	6.0
heating ΔS (J·K^{-1}·kg^{-1})	151.5	49
heating ΔS (J·K^{-1}·mol^{-1})	62.2	15.5
N, $\Delta S = R \ln(N)$	881[a]	6
fwhm (°C)	7.7	3.4
	TEA FBC	**TMA FBC**
peak onset, cooling (°C)	105	109
cooling ΔH (J·g^{-1})	65.5	18
cooling ΔH (J·mol^{-1})	24.4	5.7
cooling ΔS (J·K^{-1}·kg^{-1})	174.0	48
cooling ΔS (J·K^{-1}·mol^{-1})	64.8	15.2
fwhm (°C)	1.4	3.6

[a]For large ΔS, the N value is susceptible to large variability with small variations in ΔS.

The area under the peaks was used to calculate the enthalpy of transition (ΔH) J·g^{-1} on heating and cooling. From this, the entropy (ΔS) J·K^{-1}·kg^{-1} could be calculated by assuming the system to be in equilibrium. The ΔH values of the transitions in TEA FBC were consistent on heating and cooling at 65.7 and 65.7 J·g^{-1}, respectively. These ΔH values together with the onset temperatures of the transition gave rise to very high ΔS values of 151.5 and 174.0 J·K^{-1}·kg^{-1}, and the hysteresis of the transition temperature increased the ΔS during cooling (Table 1). It is worth noting that while the transition temperature on heating was very stable, with little variation observed between samples or heating cycles, the transition on cooling was unstable and the onset temperature varied by up to ±15 °C between different temperature cycles. The origin of this variability was unknown but may relate to the fact that the transition on cooling occurred rapidly and thus small changes in thermal history, grain size, surface morphology, and defect
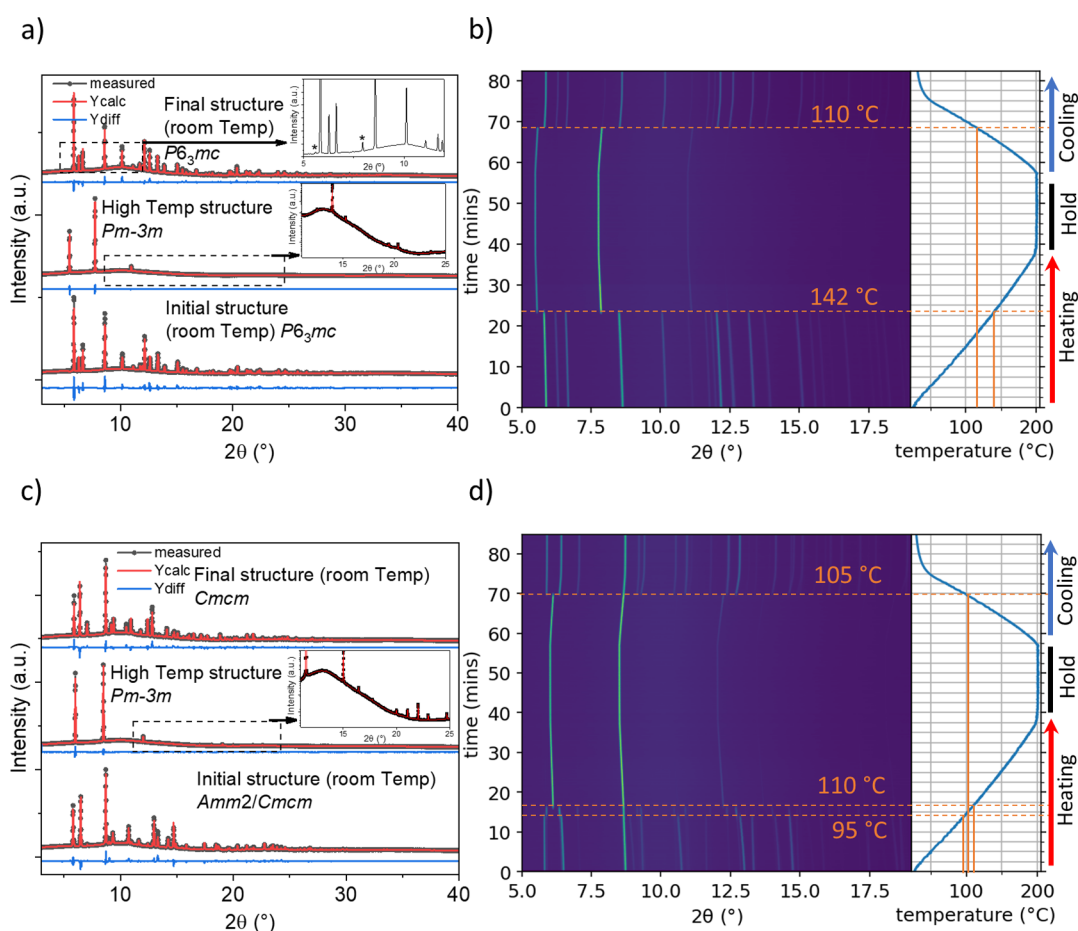
Figure 3. (a,b) TEA FBC and (c,d) TMA FBC. (a,c) Rietveld fitted powder diffraction patterns at room temperature before (bottom) and after (top) heating and in the mesophase state (middle) with plots showing data (black), fits (red), and difference profiles (blue). The insets highlight region 11−25° 2θ of mesophase diffraction with intensity on a log scale, and the existence of mesophase peaks from 5 to 12° 2θ, marked with *, in the *P6₃mc* phase region at 70 °C on cooling. (b,d) 2D contour plots of XRD patterns as a function of time, which correspond to the temperature profile on the right-hand side. Dashed lines provide a guide for the eye to determine phase transition temperatures.

concentration may influence the nucleation energy and thus transition onset temperature.

Considering that the entropy change (ΔS) of the transition is only associated with new molecular configurations, ΔS was used to estimate a change in the atomic configuration number (N) of the material using the Boltzmann equation (eq 1)

$$\Delta S = R \ln(N) \tag{1}$$

where R is the gas constant. N was related to the number of possible molecular orientational configurations in the plastic crystal.[39]

The configuration number N of the TEA FBC mesophase was very large and ranged between 1730 and 880 over multiple measurements and thermal cycles, large compared to many similar organic−inorganic plastic crystals, but smaller than many fully organic systems.[39] The variability was related to the fact that N is an exponent of a large ΔS, so variations of ± 10 J· K^{-1}·kg^{-1} (6%) cause large changes. This value shows that the mesophase transition is a severe order−disorder transition occurring within a narrow temperature range. The physical interpretation is that the mesophase exhibits many energetically equivalent molecular orientations with a flat free energy landscape between states.[40] Structurally such a state may be visualized by rotating each molecule through small Euler angles with each position representing a new orientational config-

uration. Such rotational states are frequently used to describe plastic crystals.

By comparison, the TMA FBC material showed a total of four phase transitions on heating in the temperature range −25 to 200 °C (Figure 2b). The mesophase transition took place at 110 °C with the other phase transitions occurring at 75, 28, and −10 °C. These transitions are related to structural transitions from the mesophase to *Cmcm*, then to *Amm*2, and finally to *Pma*2 orthorhombic space groups.[17,41] Unlike TEA FBC, the TMA FBC mesophase transition exhibited little hysteresis (<1 °C), with a similar fwhm on heating and cooling, and a high degree of stability with thermal cycling.

The solid−solid transition in TMA FBC from *Cmcm* to *Amm*2 showed large hysteresis (47 °C) with the transition taking place at 75 °C on heating and 28 °C on cooling. This transition was slow and diffuse on cooling, meaning a temperature region existed from approximately 30 to −10 °C where phase coexistence occurred. This type of phase coexistence where a higher-temperature phase is stabilized into a lower-temperature region is reported for other plastic crystals and is thought to be similar in nature to quench stabilized glassy phases in glass forming materials, as a degree of structural disorder inherent to the higher-temperature phases persists below the phase transition.[42]

The mesophase transition of TMA FBC had a consistent ΔH on heating and cooling of 19 and 18 J·g^{-1} and ΔS of 49 and 48 J·K^{-1}·kg^{-1} (Table 1). The resulting configuration number N for the heating transition was 6, comparable to other plastic crystals with similar compositions.[7,14] The ΔH and ΔS values for TMA FBC were less than one-third of TEA FBC, which was reflected by the large difference in the configuration numbers.

The different transition entropies of the two materials must be derived from the different functional groups, ethyl and methyl, respectively, for TEA FBC and TMA FBC because comparison with the literature shows that supramolecular crystals with the $P6_3mc$ crystal structure do not inherently possess large ΔS at the mesophase transition.[43] The functional groups influence the shape and size of the organic cation, the lattice parameters, and the strength of electrostatic, van der Waals, and halide-hydrogen intermolecular bonding interactions. The much larger ΔS of TEA FBC is thus interpreted as both the cation and anion exhibiting many energetically equivalent orientations and thus a large configurational entropy, enabled in this structure by the pseudo-spherical volume of the rotating cation, the lack of steric impedance in the structure, and the weak near isotropic bonding interactions. By comparison, the TMA FBC also goes through an order–disorder transition with an increased orientational disorder of the molecules, but the space available for rotation and the strength of the bonding interactions restrict the number of energetically equivalent orientations and thus reduce the configurational entropy.

The thermodynamic parameters of both materials reflect their potential for application in solar TES. Materials suitable for industrial solar TES require mesophase transitions in the temperature range 120–400 °C,[44] while domestic applications need lower temperatures of 25–170 °C,[45] both consistent with the mesophase transitions of TEA FBC and TMA FBC, respectively. Further requirements for solar TES applications are high ΔH and high hysteresis of the transition temperature.[46] TEA FBC, in particular, has promise due to its ΔH (65.7 J g^{-1}), which is considerably larger than that of similar halometallate materials recently reported.[14,39]

If we assume that the main cause of free energy change at the mesophase transition is the molecular orientational order, two scenarios exist for explaining the different thermodynamic changes in the two materials. First, that the mesophase state of TEA FBC has a higher degree of orientational freedom compared to TMA FBC. Second, that the $Cmcm$ solid phase prior to the mesophase in TMA FBC has a higher entropy compared to the hexagonal $P6_3mc$ solid phase before the mesophase in TEA FBC and thus lowers the ΔS of the mesophase transition.

Long-Range Structure. To understand the origin of the thermodynamic changes observed in the two materials, it was necessary to look at the structure surrounding the transition. Structural analysis using in situ XRD as a function of temperature was performed up to 200 °C. Figure 3 shows powder diffraction profiles, first at a single temperature together with the Rietveld structural fit and difference profiles and then across the full temperature range. Fits for both materials and all temperatures achieved average R_{wp} values of 2.9 ± 0.5 (standard deviation).

The TEA FBC exhibited the hexagonal $P6_3mc$ crystal structure shown in Figure 1a at room temperature (Figure 3a).[15,38] In the mesophase, the material adopted a high

symmetry structure approximated to cubic $P\bar{4}3m$ and then returned to the $P6_3mc$ structure on cooling. During heating, the structure underwent the mesophase transition abruptly at 142 °C, taking approximately 8–10 °C and 40–50 s, to complete (Figure 3b). On cooling, the transition took place abruptly at 110 °C and was apparently complete in just 2 °C or 10 s. This was in good agreement with the DSC measurements.

The XRD data, however, revealed that 30 wt % of the mesophase did not transition back to $P6_3mc$ at the initial transition temperature, but instead remained in coexistence with the $P6_3mc$ phase as a residual disordered/high temperature phase until lower temperatures. The main evidence for this was the persistence of the mesophase peaks at approximately 5.5 and 8.0° 2θ, highlighted by stars in the upper inset in Figure 3a. The in situ diffraction data showed that the remaining residual mesophase gradually transitioned back to $P6_3mc$ as the temperature reduced from 110 to 30 °C, returning to 100 wt % $P6_3mc$ phase at room temperature.

The TEA FBC mesophase exhibited few visible Bragg peaks, but those that were visible were narrow with low fwhm (Figure 3a). The small number of visible peaks indicates a high symmetry, while the narrow peak width suggests little strain in the lattice, that is, highly uniform lattice parameters throughout the crystal. Below 11° 2θ, the two visible peaks had a high intensity, indicative of a high degree of crystallinity. Above 11° 2θ, however, the peak intensity reduced sharply (Figure 3a, final structure, inset). The peak intensity reflects the distribution of positions of molecules or atoms relative to their lattice points and thus the decline in peak intensity which is related to the molecular orientational disorder.[25] Interestingly, the decreasing peak intensity with the increase in 2θ is analogous to a severe thermal vibration effect. For thermal vibration, atoms are treated as though their location oscillates around a fixed site in the crystal lattice, which results in an intensity reduction in the higher order hkl diffraction lines.[25,47] In the plastic crystals, this effect originates from the molecular orientational disorder.

Rietveld refinement of mesophase diffraction lines was carried out using a cubic $Pm\bar{3}m$ structure. The $[FeBrCl_3]^-$ anion was simulated by placing Fe at the body center location of the unit cell coordinated by two sets of energetically equivalent Cl/Br tetrahedral positions. For the organic cation, N was placed at the corners of the unit cell coordinated by two sets of C tetrahedral positions (Figure 4). The occupancies of

Pm-3m

● N ● C ● Fe ● Cl/Br
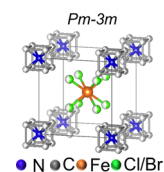
Figure 4. Mesophase structural model, cubic $Pm\bar{3}m$ with two sets of equivalent positions for the tetrahedral positions.

the equivalent positions were set to 50% to account for the stoichiometry. Thermal parameters were refined to simulate the orientational disorder.[25] This approach provides only an approximation of the structure, but we note that similar approaches in the literature have yielded similar high symmetry structures.[17] Orientational disorder of the mesophase does not cause a distribution of the lattice parameters but rather a highly uniform high symmetry lattice with a thermal vibration-like disorder of the atomic positions.[25]

TMA FBC before heating was a mixture of two phases, 90 wt % orthorhombic *Amm*2 and 10 wt % orthorhombic *Cmcm* (Figure 3c). Between 90 and 95 °C, TMA FBC underwent a solid−solid phase transition to 100 wt % *Cmcm* before the mesophase transition began at 105 °C, clearly seen in the 2D diffraction plot (Figure 3d). The mesophase transition was abrupt and took 10 °C, or 50 s, to complete.

On cooling, the mesophase transition was visible at 105 °C (Figure 3d), and the fitting showed that the material was in the *Cmcm* phase at room temperature with no evidence of residual mesophase (Figure 3c). The findings were consistent with the DSC data, which showed strong hysteresis in the *Cmcm-Amm*2 transition on cooling. The diffuse nature of this transition and its proximity to room temperature may explain the multiphase state of TMA FBC prior to the experiment, as some residual *Cmcm* may remain from the crystallization process.

The Bragg diffraction pattern of the mesophase of TMA FBC was similar to that of the TEA FBC. There were two major narrow diffraction lines with high intensity, indicating high crystallinity and little lattice strain. Above 10° 2θ, the line intensity decreased significantly due to molecular orientational disorder and structural fitting, similar as for TEA FBC, and led to an approximate structure of cubic $Pm\overline{3}m$. However, there were a number of additional diffraction lines in the 2θ range 11−25° visible in the diffractogram of TMA FBC (see Figure 3c inset). These additional diffraction lines were evidence for a more long-range structural order and lower symmetry in the TMA FBC mesophase compared to TEA FBC, despite both phases able to be approximated as the same $Pm\overline{3}m$ structure. Because the long-range structural symmetry of the mesophase is inherently linked to the local molecular orientational disorder, it is likely that additional Bragg diffraction lines indicate that TMA FBC has a lower degree of orientational freedom, with respect to TEA FBC, thus, partly explaining the lower ΔS of the mesophase transition.

The lattice parameters of all the phases in each material were determined by sequential batch fitting of each XRD pattern as a function of temperature (Table 2). The TMA FBC mesophase lattice parameters were smaller than that of TEA FBC, which was expected due to the smaller $[(CH_3)_4N]^+$ cation used in the structure and also evident by the higher 2θ position of the main Bragg peaks (Figure 3). The lattice parameters as a function of temperature were used to calculate the thermal expansion coefficients (α) for the individual crystal lattice directions of each phase. The Principal Axis Strain Calculations (PASCal) web tool was used to generate an axis-dependent strain for each phase of both materials.[48] The lattice-dependent α is important as the orientational freedom of molecular species in the structure is thought to be influenced by the available space, that is, by steric hindrance. Thus, thermal expansion may indicate how free energies change in specific cartesian planes, indicating possible driving forces for phase transitions. The thermal expansion of the $P6_3mc$ phase of TEA FBC was anisotropic, with the largest α parallel to the c axis and the polarization direction. The *Amm*2 phase of TMA FBC also exhibited the largest α parallel to c but exhibited the highest degree of α anisotropy. The c lattice parameter significantly increased in TMA FBC through the *Amm*2 to *Cmcm* phase transition (Table 2) and α parallel to the c axis was significantly reduced after the transition. In the *Cmcm* phase, α was largest in the a direction and smallest in c. Both materials expanded isotropically in the mesophase with

Table 2. Lattice Parameters Determined from Fitting Structural Models of Each Crystallographic Phase to Bragg Diffraction Lines for Each Material TEA FBC and TMA FBC

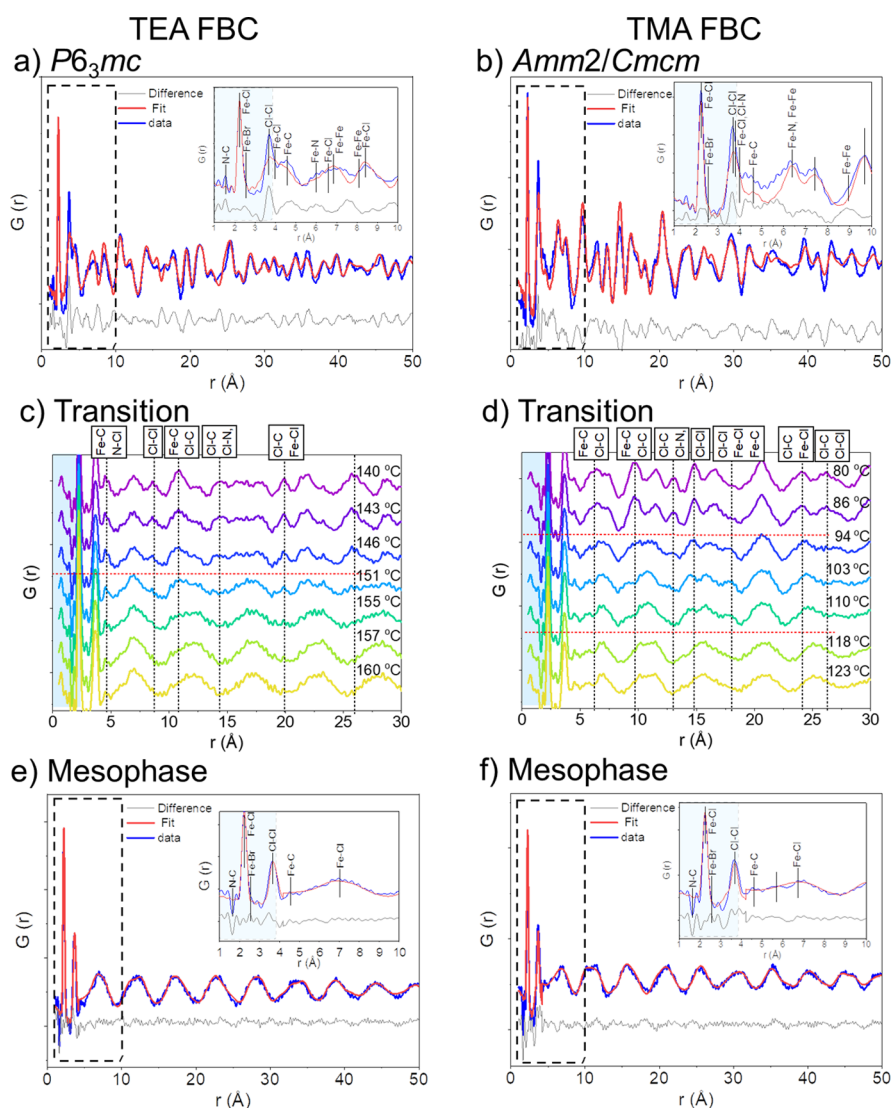|	TEA FBC		TMA FBC	
	$P6_3mc$		*Amm*2	
room temperature (24 °C)	lattice parameters (Å)	thermal expansion coefficient, α (10⁻⁶ K⁻¹)	lattice parameters (Å)	thermal expansion coefficient, α (10⁻⁶ K⁻¹)
a	8.256	107.9	7.228	34.1
b	= a	= a	8.998	87.7
c	13.305	138.4	9.313	218.6

	TMA FBC	
	Cmcm	
intermediate phase (90 °C)	lattice parameters (Å)	thermal expansion coefficient, α (10⁻⁶ K⁻¹)
a	9.035	178.5
b	9.687	110.4
c	14.280	40.3

	TEA FBC		TMA FBC	
	$Pm\overline{3}m$		$Pm\overline{3}m$	
mesophase (200 °C)	lattice parameters (Å)	thermal expansion coefficient, α (10⁻⁶ K⁻¹)	lattice parameters (Å)	thermal expansion coefficient, α (10⁻⁶ K⁻¹)
a	7.654	173.6	6.978	178.7

an increased α with respect to the immediately preceding phases.

Local Structure. In situ total X-ray scattering measurements were conducted as a function of temperature and used to produce PDFs to visualize the local structure and the orientational disorder introduced at the mesophase transition (Figure 5). At radial distances below approximately 4 Å, highlighted by the blue shading in Figure 5, the PDFs showed contributions from only the intramolecular atomic distances. The intramolecular distances were nearly identical for both materials, with the common $[FeBrCl_3]^-$ anion and similar N−C bond lengths of both $[(C_2H_5)_4N]^+$ and $[(CH_3)_4N]^+$ cations. The most dominant peaks came from Fe−Cl and Cl−Cl pairs at 2.18 and 3.54 Å, respectively (Figure 5a,b). The Fe−Br distance was visible as a small shoulder to the right of the Cl−Cl peak and an N−C distance was perhaps visible near 1.50 Å; however, the data at short bond lengths is susceptible to incomplete Fourier transforms. The smaller mass of the C and N atoms means that they only weakly scatter X-rays and thus give weak contributions to the PDFs.

From 4 to 10 Å, the PDFs included intermolecular atomic distances present in a single unit cell. In this region, the PDFs of the two materials start to differentiate from each other. The three main peaks visible come mostly from contributions of Fe−C, Fe−Cl, and Fe−Fe pairs (Figure 5a,b). In TMA FBC, the peaks are shifted to slightly lower r(Å) values and squashed together, reflecting the smaller unit cell compared to TEA FBC. Selected room-temperature atom pair distances occurring over a single unit cell are given in Table 3.

From 10 to 50 Å, the PDFs show atom pair distances occurring across multiple unit cells. As the number of possible pairs increased exponentially, straightforward correlations between peaks and specific atomic distances were difficult.

Figure 5. PDFs for (a,c,e) TEA FBC and (b,d,f) TMA FBC. (a,b) Room-temperature PDF with data, fit, and difference plots. (c,d) Multiple PDFs at different temperatures spanning the solid-to-mesophase transitions in each material. (e,f) Mesophase PDF at 170 °C for both materials with the data, fit, and difference plots. Insets highlight the *r* range inside the dashed boxes, blue shaded regions mark the intramolecular distance <4 Å, horizontal dashed lines mark the transition temperatures, and vertical dashed lines guide the eye over regions of the PDF that change significantly during the transition.

The PDFs of the two materials also diverged in this region, each having their own unique profile.

As the temperature was increased, no significant changes were visible in the interatomic distance region below 1−4 Å, confirming that no significant changes in the molecular symmetry took place (Figure 5c,d). The mesophase transitions of both materials were identified by the PDF profiles above 4 Å, evolving from having many distinguishable peaks to only broad diffuse peaks. The result was that the PDFs of the mesophase had periodic profiles reminiscent of wavefunctions. Such shapes are related to the increased molecular orientational freedom present in the mesophase, consistent with the concept of increased configurational entropy as discussed with respect to the entropy change.[25,47]

The molecular center of mass remains fixed at the crystal lattice site. Fe is located approximately at the $[FeBrCl_3]^-$ center, with some asymmetry due to the single Br, while N is located at the center of the cations. Increased orientational freedom of each molecule results in a probability distribution

of the location of other atoms (i.e., Cl, Br, and C) around the center of mass. This produces a corresponding distribution of atomic pair distances. The more the orientational disorder, the smoother the distribution of atomic distances and thus the more wave-like the PDFs.[25] However, in practice, structural models that incorporate multiple orientational configurations, let alone many orientations rotated through discrete Euler angles, are difficult to realize. In the absence of such models, the effect of probability distributions of atomic positions and the corresponding distribution of intrinsic atomic correlations can be emulated by refining the thermal factors for the atomic positions. An approach routinely utilized for the fitting of plastic crystal mesophase structures.[25]

The $P6_3mc$-to-mesophase transition in TEA FBC was observed by the evolution of the PDFs collected between 150 and 160 °C (Figure 5c). Several peaks reduced in intensity or completely disappeared, including peaks at 4.5 Å related to the Fe−C and N−Cl, 7.5 Å related to Cl−Cl, 11 Å correlated with Fe−C and Cl−C, 14 Å associated with Cl−N and Cl−C,

Table 3. Key Inter- and Intramolecular Atomic Distances in TEA FBC and TMA FBC Obtained from the Structural Models of Each Composition

material	structure	molecule	atomic species	distance (Å)
TEA FBC	$P6_3mc$	intramolecular		
		$[FeBrCl_3]^-$	Fe−Cl	2.18
			Fe−Br	2.54
			Cl−Cl	3.55
			Cl−Br	3.90
		$[(C_2H_5)_4N]^+$	N−C1	1.55
			N−C2	2.54
			C1−C2	1.65
		intermolecular		
		$[FeBrCl_3]^-$	Fe−Fe	6.66, 8.26, 10.61, 13.93
			Fe−Cl	6.61, 8.53, 10.12
		$[FeBrCl_3]^-$, $[(C_2H_5)_4N]^+$	Fe−N	5.77, 5.86,
TMA FBC	$Amm2$	intramolecular		
		$[FeBrCl_3]^-$	Fe−Cl	2.18, 2.18
			Fe−Br	2.54
			Cl−Cl	3.54
			Cl−Br	3.90
		$[(CH_3)_4N]^+$	N−C	1.46, 1.46, 1.47
		intermolecular		
		$[FeBrCl_3]^-$, $[(C_2H_5)_4N]^+$	Fe−C	4.40, 4.89
			Fe−N	5.28, 5.82, 6.55, 10.42, 11.12,
			Cl−N	4.85, 7.06
		$[FeBrCl_3]^-$	Fe−Cl	4.34,
			Fe−Fe	6.47, 8.99
			Cl−Cl	3.94, 6.47, 6.89,

and at 20 Å associated with Cl−C and Fe−Cl distances. This indicated that both anions and cations experienced an increased orientational disorder across the mesophase transition.

The PDFs of TMA FBC showed two phase transitions taking place as expected, first from *Amm*2 to *Cmcm* at 90 °C, followed by *Cmcm* to mesophase at 110 °C (Figure 5d). Peaks at 9.5 and 13 Å diminished in intensity through the *Amm*2-to-*Cmcm* transition and were related to Fe−C, Cl−C, and Cl−C, respectively, suggesting that only an orientational disordering of the cation took place. Peaks at 15 and 17 Å, related predominantly to Cl−Cl distances, only diminished at the *Cmcm*-to-mesophase transition at 110 °C, revealing that anion orientational freedom was introduced only at the mesophase transition.

TMA FBC mesophase PDFs noticeably exhibited more deviation from a wave-like profile compared to TEA FBC (Figure 5f). In previous studies, the wave-like function has been simulated by rotating the molecules of the structural model through randomly assigned Euler angles to create the effect of total orientational freedom.[47] Deviation from an ideal wave-like periodicity was thus considered to result from a lower orientational disorder in the TMA FBC structure compared to TEA FBC. Tracing the vertical dashed lines in Figure 5d showed that some correlation exists between deviation from a sinusoidal-like profile and the peaks associated with Cl−Cl pairs. This indicated that the anion

orientational freedom was lower in TMA FBC compared to TEA FBC.

The position of the wave-like diffuse peaks correlated with an approximate integer multiple of the distance between Fe−N pairs, 6.5 and 5.9 Å, for TEA FBC and TMA FBC, respectively, which was approximately half the (111) distance of the *P4/mmm* unit cell. This shows that the periodicity of the mesophase PDFs was related to the unit cell parameters of each material.

Dielectric Properties and Impedance Spectra. The dielectric and electrical properties of each material were explored using DFT. Figure 6a,b displays the influence of rotational configuration/index of both $[(CH_3)_4N]$ and $[(C_2H_5)_4N]$ anions on the dielectric constant and fundamental electronic band gap, respectively, for both TEA FC and TMA
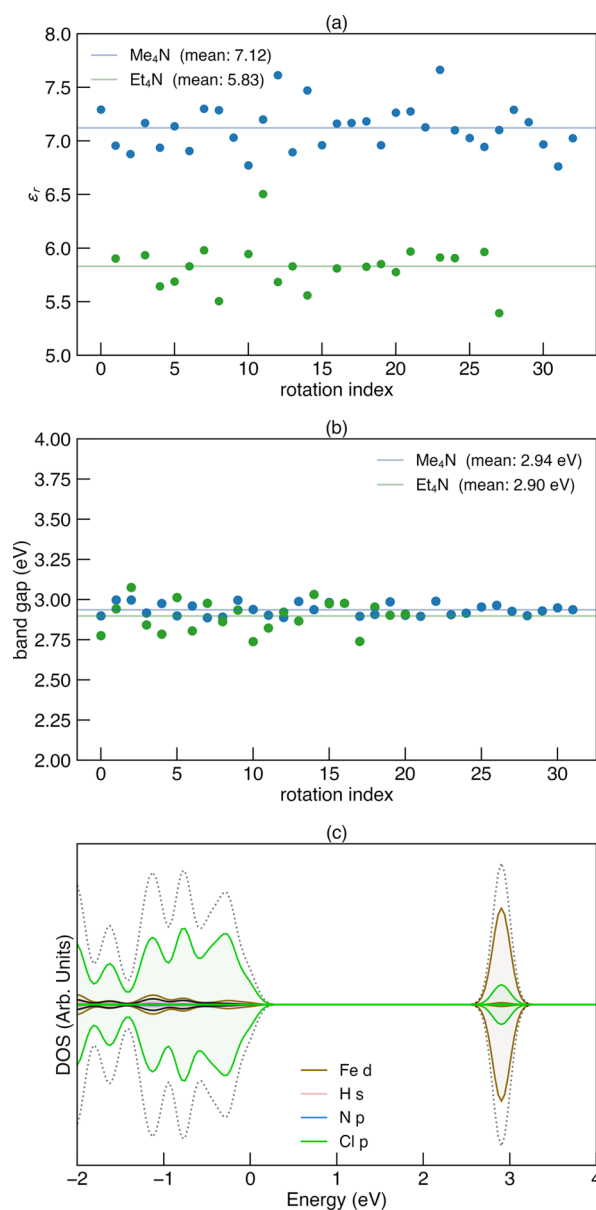
Figure 6. (a) DFPT-calculated dielectric constant and (b) band gap as a function of rotational index (configuration) for TEA FBC and TMA FBC. Rotational index indicates molecular orientations varied by rotating the molecule through sequential Euler angles. (c) Representative DOS for index 0 of TMA FBC.
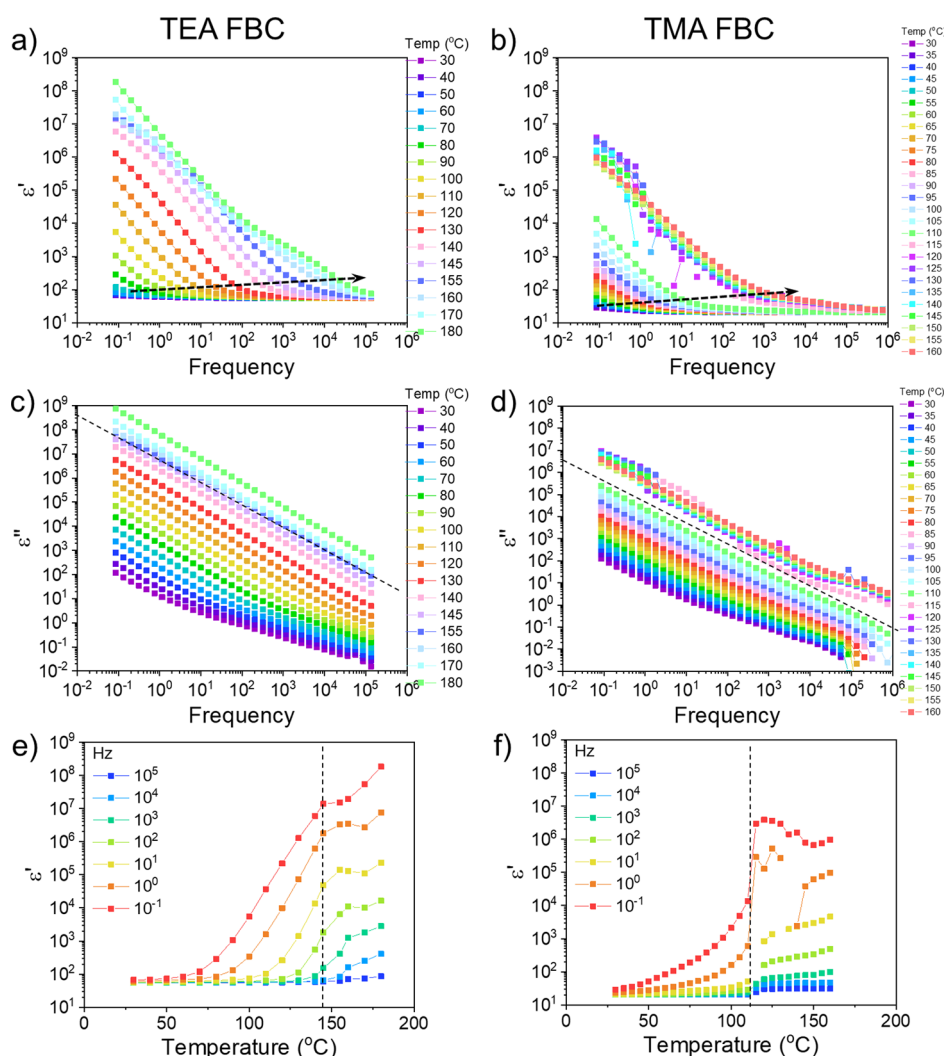
Figure 7. (a,c,e) TEA FBC and (b,d,f) TMA FBC. (a,b) Real permittivity and (c,d) imaginary permittivity as a function of frequency for different temperatures. (e,f) Real permittivity as a function of temperature for different frequencies. Arrows indicate the shift in the inflection point of ε' as temperature increases, while the dashed lines mark the location of the phase transition.

FC. Rotational configurations/indexes are created based upon unique 90° Euler rotations in the a, b, and c planes for both anions (where the rotation center is the N atom). Figure 6c shows a representative density of states (DOS)—TMA FC (rotational index = 0), for brevity, as the electronic structures between both compounds and their rotational configurations are largely similar. The DOS shows that the valence band maximum (VBM) centered at 0 eV is predominantly Cl p states, and the conduction band minimum (CBM) comprises mixing between Fe d states and Cl p, showing that the single element ions (Fe^{3+}, Cl^-) in the structure play the major role in the determination of the electronic structure around Accessible Fermi levels, as opposed to the molecular ions.

Our results indicate that rotational configurations result in small fluctuations to the dielectric constant, likely due to the distortion of the $[FeCl_4]$ anion, giving rise to values of 5.13 and 7.12 for TEA FC and TMA FC. The value for TMA FC matches well with the low-temperature, low-frequency dielectric constants from previous experimental literature ~6−7.[17] Similar results are seen in terms of the electronic structure and band gap of TMA FC and TEA FC, whereby the rotational disorder of the organic cation does not have a significant influence. The DOS indicates that the band edges of

these materials are dominated by the electronic states of the $[FeCl_4]$ anion, resulting in the fundamental band gaps of TMA FC and TEA FC being around ~2.94 and ~2.90 eV, respectively, corresponding well with the translucent yellow coloring seen in experimental samples in the literature.[17] This band gap is also highly consistent with that reported for the optical band gap determined from solid-state UV−vis spectroscopy and is derived from the inorganic anion.[49]

The frequency and temperature dependence of the permittivity of the two materials revealed the electronic fingerprint of their transition from an ordered dielectric to a locally disordered plastic crystal (Figure 7). The real permittivity (ε') of TEA FBC at room temperature showed a typical plateau between 10^4 and 1 Hz with a value of around 60 before increasing in the low-frequency range due to dielectric losses and conductivity (Figure 7a). As the temperature increased from 30 to 155 °C, the ε' showed a systematic increase in the low-frequency value and an increase of the frequency at which an inflection in the ε' occurred (marked by an arrow in Figure 7a). Above the mesophase transition temperature at 150 °C, the ε' exhibited a step-like increase distinct from the incremental changes seen at lower temperatures. TMA FBC showed similar behavior, but with a

plateau in the ε' at approximately 20 (Figure 7b). The incremental increase in the low-frequency values and the shift of the inflection point to higher frequencies also occurred. A larger step-like increase was observed between 110 and 115 °C at the mesophase transition. Dimensional instability and electrode degradation was observed above the mesophase transition in both materials, and thus, the discussion is focused on data leading up to and including the phase transition.

The imaginary impedance (ε'') of both materials was similar, with a relaxation at lower temperatures between 10^2 and 10^4 Hz, gradually replaced by a linear increase from high to low frequencies (Figure 7c,d). The TEA FBC ultimately reached higher ε'' values relative to TMA FBC, although their magnitudes were similar at comparable temperatures.

The increase in ε'' as a function of temperature was indicative of reducing resistivity and increasing dielectric loss.[37] The increase seen across the mesophase transition in both materials, but more visible in TMA FBC, was consistent with the plastic crystal literature, which shows that ionic conductivity is significantly increased in the mesophase.[50,51] This ionic conductivity increase is explained in part by the orientational freedom of molecular species which allows for free energies to be minimized during the transport of charge carriers.

The ε' as a function of temperature showed some differences in the temperature dependence of the two materials (Figure 7e,f). The TEA FBC exhibited a small increase in ε' until 60 °C at which point the lower frequency data increased almost exponentially until the transition onset at 150 °C. There was a plateau until 160 °C before again increasing. The ε' of TMA FBC by comparison, increased more rapidly in the region below 50 °C and then more gradually up to the transition at 110 °C. The transition exhibited a step-like increase, followed by a plateau. The broken data set at 10^{-1} and 10^0 Hz frequencies were the result of very low resistivity at high temperatures.

To further investigate the dielectric behavior of the two materials, the negative of the imaginary component of the impedance ($-Z''$) was examined (Figure 8). The decrease in the impedance and increase of the bulk relaxation frequency was visible as the temperature increased between 30 and 140 °C for TEA FBC and between 30 and 120 °C for TMA FBC (Figure 8a,b). In both materials, a second peak at lower frequencies emerged. This could have been the result of grain boundary, electrode interface effect, or a second bulk relaxation mechanism.[42] In both materials, at temperatures coinciding with their mesophase transition the impedance behavior became irregular, likely relating to the high conductivity.

$$\tau = \frac{1}{\omega_{p1}} \tag{2}$$

The relaxation times were plotted in an Arrhenius plot in Figure 8c and using eq 3, the activation energy of relaxation (φ) was estimated.[52,53]

$$\tau = \tau_0 \exp\left(\frac{\varphi}{K_B T}\right) \tag{3}$$

The activation energies of relaxation were estimated by making linear fits that divided the graph into two sections, the first from 30 to 90 °C and the second from 90 to 120 °C (Figure 8c). The TMA FBC material underwent the transitions from $Amm2$ to $Cmcm$ between 70 and 90 °C, so it was
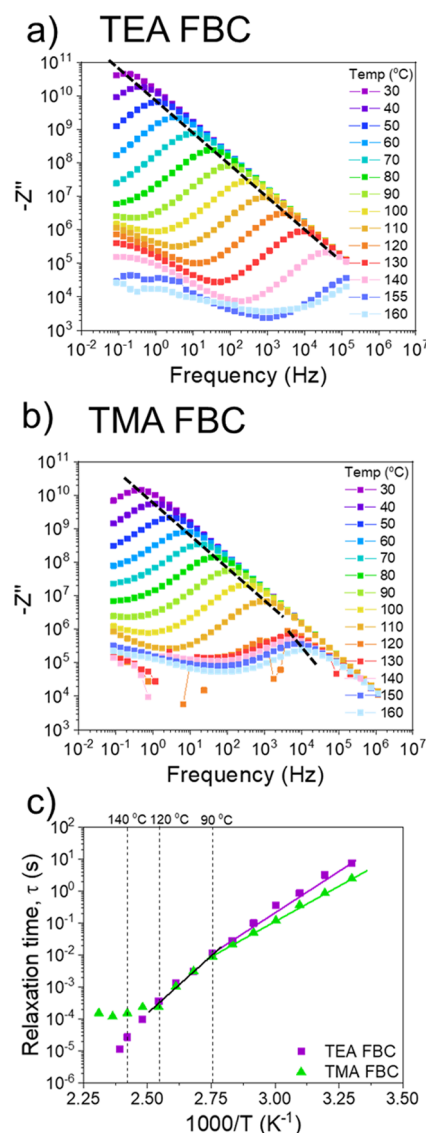
Figure 8. Negative imaginary impedances ($-Z''$) for (a) TEA FBC and (b) TMA FBC. Dashed lines are a guided to the eye along the relaxation peaks. (c) Relaxation times determined from major $-Z''$ relaxation frequency for TEA FBC and TMA FBC. Solid lines are a guide to the eye for each temperature region, 30−90 and 90−120 °C, as divided by dashed lines.

appropriate to find a transition point in the relaxation time curves near this temperature. For comparability, TEA FBC was also divided in the same manner, and while there was no structural justification for this, it does fit well with the change observed in ε', from gradual to more rapidly increasing as a function of temperature (Figure 7e). Activation energies are given in Table 4.

The activation energies for bulk conductivity were also estimated from DC current−voltage ($I-V$) measurements (Figure 9). TEA FBC exhibited asymmetric conductivity as a function of field direction (Figure 9a), while TMA FBC was symmetric (Figure 9b). Leakage currents at comparable temperatures were lower in TEA FBC compared to TMA FBC, for example, 5.02 and 5.38 $\mu A/cm^2$ at 5 kV/cm and 100 °C, respectively.

The conductivity at the maximum electric field was made into an Arrhenius plot to determine the activation energy of

Table 4. Activation Energies Determined from Relaxation Times of the Main $-Z''$ Relaxation Peak (φ), Purely Resistive Component of the Cole−Cole Relation ($E_{a,AC}$), and DC Conductivity ($E_{a,DC}$)

		TEA FBC	TMA FBC	
φ, 30−90 °C (eV)		1.05	0.88	
φ, 90−120 °C (eV)		1.38	1.48	
φ, 120−160 °C (eV)			0.38	
	TEA FBC		TMA FBC	
	positive bias	negative bias	positive bias	negative bias
$E_{a,DC}$ (eV) < 100 °C	0.76	0.86	0.98	0.99
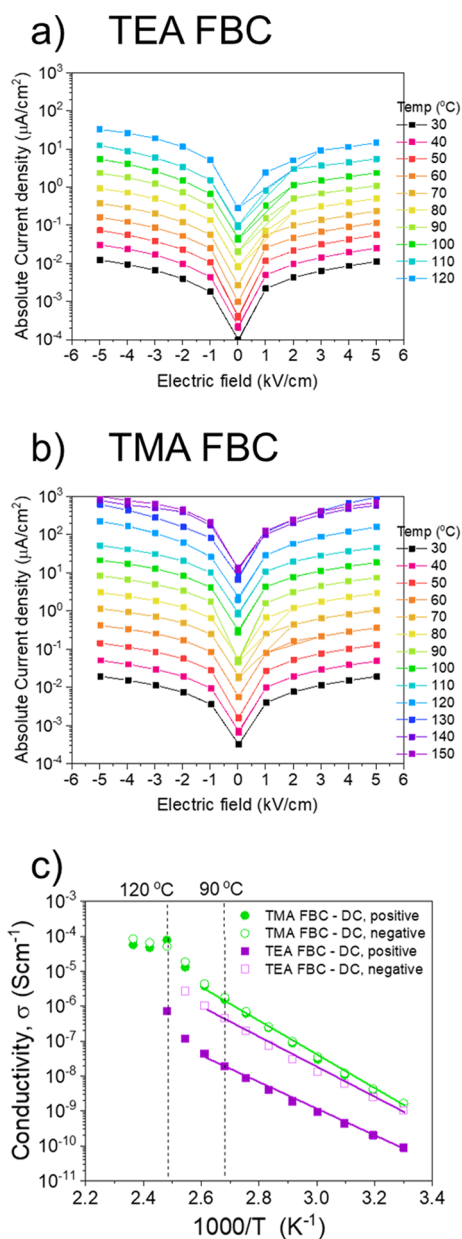
Figure 9. DC leakage current data for (a) TEA FBC and (b) TMA FBC. Absolute current density is plotted on a log scale as a function of temperature. (c) Arrhenius plot for both materials with log conductivity vs $1000/T$. Dashed vertical lines mark the distinct transition points, also marked in Figure 8c, and colored full lines are linear fits.

DC conductivity, $E_{a,DC}$ (Figure 9c). The asymmetry of TEA FBC I−V curves resulted in an $E_{a,DC}$ that was lowest in the positive field direction. This was also supported by the fact that the $E_{a,DC}$ was lower than $E_{a,AC}$ and φ (Table 4). The reason for this was thought to be an electrode/sample interface effect, specifically an interfacial blocking force to ionic conduction. TMA FBC, however, exhibited little variation between the $E_{a,DC}$, $E_{a,AC}$, and φ values.

In ionic plastic crystals such as these, we anticipate that electrical conductivity in the bulk can be both ionic and electronic, enabled by three mechanisms: (1) defects or vacancies in the crystal lattice, (2) orientational disorder of the molecular ions, and (3) conformational disorder; meaning grain boundaries, slip planes, or dislocations.[42,54,55] In stoichiometric materials, ionic conductivity should be intrinsic and mediated by vacancy or defect formation. This is likely the main mechanism behind the temperature-dependent loss behavior independent of the phase transitions. Activation energies of 0.7−1.0 eV in their room-temperature phases of for both materials indicated ionic conduction mediated by defects to be the primary mechanism. This agreed with that of similar material systems, such as lead iodide perovskites.[56] The slightly lower $E_{a,DC}$ for TEA FBC may be caused by weaker intramolecular bonding in the larger $P6_3mc$ unit cell which is, in turn, related to the larger size of the $[(C_2H_5)_4N]^+$ cation, compared to that of $[(CH_3)_4N]^+$.

Changes in conductivity across the $Amm2$ to $Cmcm$ phase transition in TMA FBC were relatively inconsequential compared to the change at the mesophase transition, which indicates that the $[FeBrCl_3]^-$ anion orientational freedom is important for the conductivity and loss behavior.

In plastic crystals, it is common for cation migration to dominate the ionic conductivity below the mesophase transition, while above the transition, both cation and anion migrations readily occur and can be responsible for large increases in ionic conductivity at the transition.[50,51] The PDF data (Figure 5) provide evidence for increased rotational freedom of both molecular ions and thus suggests that both ions may be mobile and able to contribute conductivity. It is also possible that halide migration, either Cl⁻ or Br⁻ with Br⁻being more labile, is involved in the ionic conductivity which implicates the involvement of FeX₃ defects (X = halide). Halide mobility is widely observed in the lead halide perovskite materials.[56]

■ CONCLUSIONS

The TEA FBC had a higher entropy change of 151.5 J·K⁻¹·kg⁻¹ through the mesophase transition, compared to 49 J·K⁻¹·kg⁻¹ for TMA FBC. The only chemical difference is the ethyl and methyl functional groups of the cations, which likely impacted the intermolecular electrostatic bond strength and halide-hydrogen bonding interactions, as well as the lattice parameters. TEA FBC has a larger unit cell in the mesophase, allowing more space for rotation and suggesting a weaker electrostatic bond strength. This was likely to result in more rotational freedom of both cation and anions in the mesophase and, as a result, a much higher ΔS of the mesophase transition. This was correlated with a lower degree of long-range structural order evidenced by XRD and a higher degree of the molecular orientational freedom of both the cations and anions introduced at the mesophase transition, with more rotational freedom evident in the cations, as seen in the PDFs. By comparison TMA FBC had some orientational disorder of

the cation introduced at the *Amm2*-to-*Cmcm* transition before the mesophase, which may have also reduced the total entropy change at the mesophase transition in TMA FBC. The mesophase structural disorder could in part be quenched into the TEA FBC *P6₃mc* structure on cooling, with 30 wt % remaining until room temperature. No such quenching was observed in the TMA FBC *Cmcm* structure. The high latent heat, transition temperatures and thermal hysteresis make both compounds promising candidates for TES applications, especially TEA FBC, which shows a large latent heat of 65.7 J g^{-1}. Impedance spectroscopy and leakage current measurements showed that increases in conductivity occurred as a function of temperature below the mesophase transition of both materials, with two temperature regions, above and below 90 °C with activation energies <1.0 and >1.38 eV, respectively. The activation energies below the transition suggested vacancy-mediated ionic conduction, supported by the band gaps determined by computation which were approximately double the activation energies at elevated temperatures, at 2.9 eV. Above the transition, both vacancy-mediated and electronic contributions are likely prevalent. The significant increase in conductivity at the mesophase transition was related to the introduction of orientational freedom of both molecular ions, with the introduction of anion orientational freedom likely to play the largest role.

■ AUTHOR INFORMATION

Corresponding Author

Julian Walker − *Department of Materials Science and Engineering, NTNU Norwegian University of Science and Technology, Trondheim 7491, Norway;* ● orcid.org/0000-0002-7780-6710; Email: julian.walker@ntnu.no

Authors

Kenneth P. Marshall − *Department of Materials Science and Engineering, NTNU Norwegian University of Science and Technology, Trondheim 7491, Norway; Swiss-Norwegian Beam Lines, European Synchrotron Radiation Facility, Grenoble 38043, France*

Jorge Salgado-Beceiro − *QuiMolMat Group, Department Chemistry, Faculty of Science and Advanced Scientific Research Center (CICA), University of A Coruña, A Coruña 15071, Spain;* ● orcid.org/0000-0001-7991-2819

Benjamin A. D. Williamson − *Department of Materials Science and Engineering, NTNU Norwegian University of Science and Technology, Trondheim 7491, Norway;* ● orcid.org/0000-0002-6242-1121

Nora S. Løndal − *Department of Materials Science and Engineering, NTNU Norwegian University of Science and Technology, Trondheim 7491, Norway*

Socorro Castro-Garcia − *QuiMolMat Group, Department Chemistry, Faculty of Science and Advanced Scientific Research Center (CICA), University of A Coruña, A Coruña 15071, Spain*

Manuel Sánchez Andújar − *QuiMolMat Group, Department Chemistry, Faculty of Science and Advanced Scientific Research Center (CICA), University of A Coruña, A Coruña 15071, Spain*

Sverre M. Selbach − *Department of Materials Science and Engineering, NTNU Norwegian University of Science and Technology, Trondheim 7491, Norway*

Dmitry Chernyshov − *Swiss-Norwegian Beam Lines, European Synchrotron Radiation Facility, Grenoble 38043, France*

Mari-Ann Einarsrud − *Department of Materials Science and Engineering, NTNU Norwegian University of Science and Technology, Trondheim 7491, Norway;* ● orcid.org/0000-0002-3017-1156

Complete contact information is available at:
https://pubs.acs.org/10.1021/acs.chemmater.1c03778

Author Contributions

The research planning and manuscript writing was carried out by J.W. with contributions from M.A.E. K.P.M. provided critical support for X-ray experiments and data analysis. N.S.L. performed some sample synthesis. J.S.B. and S.C.G. provided input on calorimetry measurements and analysis. DC provided support for experiments and data from the ESRF. B.A.D.W. performed computational experiments with support from S.M.S. All authors reviewed, edited, and contributed to the manuscript.

Notes

The authors declare no competing financial interest.

■ ACKNOWLEDGMENTS

■ ABBREVIATIONS

TEA FBC, tetraethylammonium bromotrichloroferrate(III); TMA FBC, tetramethylammonium bromotrichloroferrate(III); ESRF, European Synchrotron Radiation Facility; SNBL, Swiss-Norwegian Beam Line

■ REFERENCES

(1) Harada, J.; Shimojo, T.; Oyamaguchi, H.; Hasegawa, H.; Takahashi, Y.; Satomi, K.; Suzuki, Y.; Kawamata, J.; Inabe, T. Directionally tunable and mechanically deformable ferroelectric crystals from rotating polar globular ionic molecules. *Nat. Chem.* **2016**, *8*, 946.

(2) Tang, Y.-Y.; Li, P.-F.; Liao, W.-Q.; Shi, P.-P.; You, Y.-M.; Xiong, R.-G. Multiaxial molecular ferroelectric thin films bring light to practical applications. *J. Am. Chem. Soc.* **2018**, *140*, 8051.

(3) Harada, J. Plastyic/ferroelectric molecular crystals: Ferroelectric performance in bulk polycrystal forms. *Apl. Mater.* **2021**, *9*, 020901.

(4) Ye, H.-Y.; Ge, J.-Z.; Tang, Y.-Y.; Li, P.-F.; Zhang, Y.; You, Y.-M.; Xiong, R.-G. Molecular ferroelectric with most equivalent polarization directions induced by the plastic phase transition. *J. Am. Chem. Soc.* **2016**, *138*, 13175.

(5) Timmermans, J. Plastic crystals: A historical review. *J. Phys. Chem. Solids* **1961**, *18*, 1.

(6) Li, B.; Kawakita, Y.; Ohira-Kawamura, S.; Sugahara, T.; Wang, H.; Wang, j.; Chen, Y.; Kawaguchi, S. I.; Kawaguchi, S.; Ohara, K.; Li, K.; Yu, D.; Mole, R.; Hattori, T.; Kikuchi, T.; Yano, S.-I.; Zhang, Z.; Ren, W.; Lin, S.; Sakata, O.; Nakajima, K.; Zhang, Z. Colossal baracaloric effects in plastic crystals. *Nature* **2019**, *567*, 506.

(7) Salgado-Beceiro, J.; Nonato, A.; Silva, R. X.; García-Fernández, A.; Sánchez-Andújar, M.; Castro-García, S.; Stern-Taulats, E.; Señarís-Rodríguez, M. A.; Moya, X.; Bermúdez-García, J. M. Near-room-temperature reversible giant baracaloric effects in [(CH$_3$)$_4$N]Mn-[N$_3$]$_3$ hybrid perovskite. *Mater. Adv.* **2020**, *1*, 3167.

(8) Pringle, J. M.; Howlett, P. C.; MacFarlane, D. R.; Forsyth, M. Organic ionic plastic crystals: recent advances. *J. Mater. Chem.* **2010**, *20*, 2056.

(9) Ibn-Mohammed, T.; Randall, C. A.; Mustapha, K. B.; Guo, J.; Walker, J.; Berbano, S.; Koh, S. C. L.; Wang, D.; Sinclair, D. C.; Reaney, I. M. Decarbonising ceramic manufacturing: a techno-economic analysis of energy efficient sintering technologies in the functional materials sector. *J. Eur. Ceram. Soc.* **2019**, *39*, 5213.

(10) Walker, J.; Miranti, R.; Skjærvø, S. L.; Rojac, T.; Grande, T.; Einarsrud, M.-A. Super-coercive electric field hysteresis in ferroelectric plastic crystal tetramethylammonium bromotrichloroferrate(III). *J. Mater. Chem. C* **2020**, *8*, 3206.

(11) Walker, J.; Scherrer, S.; Løndal, N. S.; Grande, T.; Einarsrud, M.-A. Electric field dependent polarization switching of tetramethylammonium bromotrichloroferrate(III) ferroelectric plastic crystals. *Appl. Phys. Lett.* **2020**, *116*, 242902.

(12) Das, S.; Mondal, A.; Reddy, C. M. Harnessing molecular rotations in plastic crystals: a holistic view for crystal engineering of adaptive soft materials. *Chem. Soc. Rev.* **2020**, *49*, 8878.

(13) King, A. H. Our Elemental footprint. *Nat. Mater.* **2019**, *18*, 408.

(14) Salgado-Beceiro, J.; Bermúdez-García, J. M.; Llamas-Saiz, A. L.; Castro-García, S.; Señarís-Rodríguez, M. A.; Rivadulla, F.; Sánchez-Andújar, M. Multifunctional properties and multi-energy storage in the [(CH$_3$)$_3$S][FeCl4] plastic crystal. *J. Mater. Chem. C* **2020**, *8*, 13686.

(15) Evans, D. J.; Hills, A.; Hughes, D. L.; Leigh, G. J. Structures of tetraethylammonium tetrachloroferrate(III) and the mixed halide iron(III) complex, [NEt$_4$][FeBrCl$_3$]. *Acta Crystallogr., Sect. C: Cryst. Struct. Commun.* **1990**, *46*, 1818.

(16) Laio, W.-Q.; Zhao, D.; Tang, Y.-Y.; Zhang, Y.; Li, P.-F.; Shi, P.-P.; Chen, X.-G.; You, Y.-M.; Xiong, R.-G. A molecular perovskite solid solution with piezoelectricity stronger than lead zirconate titanate. *Science* **2019**, *363*, 1206.

(17) Harada, J.; Yoneyama, N.; Yokokura, S.; Takahashi, Y.; Miura, A.; Kitamura, N.; Inabe, T. Ferroelectricity and Piezoelectricity in Free-Standing Polycrystalline Films of Plastic Crystals. *J. Am. Chem. Soc.* **2018**, *140*, 346.

(18) Wyrzykowski, D.; Pattek-Janczk, A.; Maniecki, T.; Zaremba, K.; Warnke, Z. Thermal properties of tetraethylammonium tetrachloro-, bromotrichloro- and tribromochloroferrates(III). *J. Therm. Anal. Calorim.* **2008**, *91*, 279.

(19) Dubois, M.-A.; Muralt, P. Properties of aluminum nitride thin films for piezoelectric transducers and microwave filter applications. *Appl. Phys. Lett.* **1999**, *74*, 3032.

(20) Trolier-McKinstry, S.; Muralt, P. Thin film piezoelectrics for MEMS. *J. Electroceram.* **2004**, *12*, 7.

(21) Liu, H.-Y.; Zhang, H.-Y.; Chen, X.-G.; Xiong, R.-G. Molecular design principles for ferroelectrics: Ferroelectrochemistry. *J. Am. Chem. Soc.* **2020**, *142*, 15205.

(22) Coelho, A. A. TOPAS and TOPAS-Academic: an optimization program integrating computer algebra and crystallographic objects written in C++. *J. Appl. Crystallogr.* **2018**, *51*, 210.

(23) Juhás, P.; Davis, T.; Farrow, C. L.; Billinge, S. J. L. PDFgetX3: A rapid and highly automatable program for processing powder diffraction data into total scattering pair distribution functions. *J. Appl. Crystallogr.* **2013**, *46*, 560.

(24) Juhás, P.; Farrow, C. L.; Yang, X.; Knox, K. R.; Billinge, S. J. L. Complex modeling: a strategy and software program for combining multiple information sources to solve ill posed structure and nanostructure inverse problems. *Acta Crystallogr., Sect. A: Found. Adv.* **2015**, *71*, 562.

(25) Shalaev, E.; Wu, K.; Shamblin, S.; Krzyzaniak, J. F.; Descamps, M. Crystalline mesophases: Structure, mobility, and pharmaceutical properties. *Adv. Drug Delivery Rev.* **2016**, *100*, 194.

(26) Kresse, G.; Hafner, J. Ab initio molecular dynamics for liquid metals. *Phys. Rev. B: Condens. Matter Mater. Phys.* **1993**, *47*, 558−561.

(27) Kresse, G.; Hafner, J. Ab initio molecular-dynamics simulation of the liquid-metal−amorphous-semiconductor transition in germanium. *Phys. Rev. B: Condens. Matter Mater. Phys.* **1994**, *49*, 14251−14269.

(28) Kresse, G.; Furthmüller, J.; Kresse, G.; Furthmüller, J. Efficient iterative schemes for ab initio total-energy calculations using a plane-wave basis set. *Phys. Rev. B: Condens. Matter Mater. Phys.* **1996**, *54*, 11169.

(29) Kresse, G.; Furthmüller, J. Efficiency of ab-initio total energy calculations for metals and semiconductors using a plane-wave basis set. *Comput. Mater. Sci.* **1996**, *6*, 15−50.

(30) Perdew, J. P.; Burke, K.; Ernzerhof, M. Generalized gradient approximation made simple. *Phys. Rev. Lett.* **1996**, *77*, 3865−3868.

(31) Perdew, J. P.; Ruzsinszky, A.; Csonka, G. I.; Vydrov, O. A.; Scuseria, G. E.; Constantin, L. A.; Zhou, X.; Burke, K. Restoring the density-gradient expansion for exchange in solids and surfaces. *Phys. Rev. Lett.* **2008**, *100*, 136406.

(32) Blöchl, P. E. Projector augmented-wave method. *Phys. Rev. B: Condens. Matter Mater. Phys.* **1994**, *50*, 17953−17979.

(33) Dudarev, S. L.; Botton, G. A.; Savrasov, S. Y.; Humphreys, C. J.; Sutton, A. P. Electron-energy-loss spectra and the structural stability of nickel oxide: An LSDA+ U study. *Phys. Rev. B: Condens. Matter Mater. Phys.* **1998**, *57*, 1505−1509.

(34) Ho-Kimura, S.; Williamson, B. A. D.; Sathasivam, S.; Moniz, S. J. A.; He, G.; Luo, W.; Scanlon, D. O.; Tang, J.; Parkin, I. P. Origin of high-efficiency photoelectrochemical water splitting on hematite/ functional nanohybrid metal oxide overlayer photoanode after a low temperature inert gas annealing treatment. *ACS Omega* **2019**, *4*, 1449.

(35) Gajdoš, M.; Hummer, K.; Kresse, G.; Furthmüller, J.; Bechstedt, F. Linear optical properties in the projector-augmented wave methodology. *Phys. Rev. B: Condens. Matter Mater. Phys.* **2006**, *73*, 045112.

(36) Herz, L. M. How lattice dynamics moderate the electronic properties of metal-halide perovskites. *J. Phys. Chem. Lett.* **2018**, *9*, 6853−6863.

(37) Wilson, J. N.; Frost, J. M.; Wallace, S. K.; Walsh, A. Dielectric and ferroic properties of metal halide perovskites. *Apl. Mater.* **2019**, *7*, 010901.

(38) Lutz, M.; Huang, Y.; Moret, M.-E.; Klein Gebbink, R. J. M. Phase transitions and twinned lowtemperature structures of tetraethylammonium tetrachloridoferrate(III). *Acta Crystallogr., Sect. C: Struct. Chem.* **2014**, *70*, 470−476.

(39) Li, D.; Zhao, X.-M.; Zhao, H.-X.; Long, L.-S.; Zheng, L.-S. Coexistence of Magnetic-Optic-Electric Triple Switching and Thermal Energy Storage in a Multifunctional Plastic Crystal of Trimethylchloromethyl Ammonium Tetrachloroferrate(III). *Inorg. Chem.* **2019**, *58*, 655.

(40) Guthrie, G. B.; McCullough, J. P. Some observations on phase transformations in molecular crystals. *J. Phys. Chem. Solids* **1961**, *18*, 53.

(41) Salgado-Beceiro, J.; Castro-García, S.; Sánchez-Andújar, M.; Rivadulla, F. Motional Narrowing of Electron Spin Resonance Absorption in the Plastic-Crystal Phase of [(CH$_3$)$_4$N]FeCl$_4$. *J. Phys. Chem. C* **2018**, *122*, 27769.

(42) Brand, R.; Lunkenheimer, P.; Loidl, A. Relaxation dynamics in plastic crystals. *J. Chem. Phys.* **2002**, *116*, 10386.

(43) Cai, H.-L.; Zhang, Y.; Fu, D.-W.; Zhang, W.; Liu, T.; Yoshikawa, H.; Awaga, K.; Xiong, R.-G. Above-room-temperature magnetodielectric coupling in a possible molecule0based multiferroic: Triethylmethylammonium tetrabromoferrate(III). *J. Am. Chem. Soc.* **2012**, *134*, 18487.

(44) Garg, H. P.; Mullick, S. C.; Bhargava, V. K. *Solar Thermal Energy Storage*; Springer Science & Business Media, 2012.

(45) Seddegh, S.; Wang, X.; Henderson, A. D.; Xing, Z. Solar domestic hot water systems using latent heat energy storage medium: a review. *Renew. Sustain. Energy Rev.* **2015**, *49*, 517−533.

(46) Sharma, S. D.; Sagara, K. Latent heat storage materials and systems: a review. *Int. J. Green Energy* **2005**, 2, 1.

(47) Jurkiewicz, K.; Glajcar, W.; Kamiński, K.; Temleitner, L.; Burian, A. Structure of 1, 6-anhydro-*β*-d-glucopyranose in plastic crystal, orientational glass, liquid and ordinary glass forms: molecular modeling and X-ray diffraction studies. *Acta Crystallogr., Sect. B: Struct. Sci., Cryst. Eng. Mater.* **2021**, 77, 138.

(48) Cliffe, M. J.; Goodwin, A. L. PASCal: A principal axis strain calculator for thermal expansion and compressibility determination. *J. Appl. Crystallogr.* **2012**, 45, 1321.

(49) Brahim, K.B.; Gzaiel, M.B.; Oueslati, A.; Khirouni, K.; Gargouri, M.; Corbel, G.; Bardeau, J.-F. Organic-inorganic inter-actions revealed by Raman spectroscopy during reversible phase transitions in semiconducting $[(C_2H_5)_4N]FeCl_4$. *RSC Adv.* **2021**, 11, 18651.

(50) Pringle, J. M. Recent progress in the development and use of organic ionic plastic crystal electrolytes. *Phys. Chem. Chem. Phys.* **2013**, 15, 1339.

(51) Alarco, P.-J.; Abu-Lebdeh, Y.; Abouimrane, A.; Armand, M. The plastic-crystalline phase of succinonitrile as a universal matrix for solid-state ionic conductors. *Nat. Mater.* **2004**, 3, 476.

(52) Souza, F. M. Electrical Conductivity in the KDP, ADP, and K1-x (NH4) xH2PO4 Crystals. *Mater. Res.* **2017**, 20, 532.

(53) Elliott, S. R. Calculation of the dc conductivity activation energy of ionically conducting glasses. *J. Non-Cryst. Solids* **1994**, 172−174, 1343.

(54) Böhmer, R.; Ngai, K. L.; Angell, C. A.; Plazek, D. J. Nonexponential relaxations in strong and fragile glass formers. *J. Chem. Phys.* **1993**, 99, 4201.

(55) Bauer, T.; Köhler, M.; Lunkenheimer, P.; Loidl, A.; Angell, C. A. Relaxation dynamics and ionic conductivity in a fragile plastic crystal. *J. Chem. Phys.* **2010**, 133, 144509.

(56) Zhao, Y.-C.; Zhou, W.-K.; Zhou, X.; Liu, K.-H.; Yu, D.-P.; Zhao, Q. Quantification of light-enhanced ionic transport in lead iodide perovskite thin films and its solar cell applications. *Light Sci. Appl.* **2017**, 6, No. e16243.